Materials Advances

ROYAL SOCIETY OF CHEMISTRY

PAPER

View Article Online
View Journal | View Issue

Cite this: *Mater. Adv.*, 2024, 5, 4753

Projection-based 3D printing of multichannel poly(caprolactone) methacrylate nerve guidance conduit for peripheral nerve regeneration†

Haibing Li, ‡[a] Ke Yao,‡[b] Yuewei Chen,[b] Wensong Ye[a] and Qiang Shu*[a]

Received 25th January 2024,
Accepted 10th April 2024

DOI: 10.1039/d4ma00073k

rsc.li/materials-advances

The repair of peripheral nerves and the restoration of the innervated function are significantly challenging for clinicians and researchers because of their limited self-regenerative capacity. Although nerve guidance conduits (NGCs) are a promising alternative, several challenges such as material selection, structural design, and fabrication methods remain to be addressed. At present, commercially available NGCs have a simple hollow structure, constrained by the use of regulatory-approved materials and conventional fabrication methods. This study used an advanced method for manufacturing NGCs by employing projection-based 3D printing to fabricate a series of 1-, 4-, and 7-channel conduits from poly(caprolactone) methacrylate (PCLMA). These were evaluated on the basis of morphologic and mechanical characteristics, through the *in vitro* culture of rat Schwann cells 96 and *in vivo* by using a 10-mm-gap repair model in Sprague-Dawley rats. The 4- and 7-channel NGCs exhibited considerably better nerve repair efficiency than the 1-channel NGCs. This observation suggests that NGCs with multiple channels have greater superiority in guiding nerve regeneration. The study offers a technological paradigm for precisely manufacturing biocompatible materials and serves as a valued reference for future advancements in more intricate NGC designs, larger scaffold dimensions with biodegradability, and more extended implantation research.

Introduction

The peripheral nerve, a crucial constituent of the nervous system, controls the sending and receiving of signals between the central nerve and peripheral organs *via* sensory and motor nerve fibers. With the increase in the number of patients with congenital defects and degenerative diseases and the prevalence of traumatic events, the morbidity rate of peripheral nerve injury (PNI) is steadily increasing each year.[1] The reconstruction of nerve structural integrity is significantly challenging, particularly in patients with irreducible nerve defects (>5 mm) where the self-regeneration capacity is limited.[2] Restoring the nerve continuity using an autologous nerve graft is a paramount consideration. However, this restoration procedure is associated with several limitations including donor site morbidity, restricted availability of donor tissue, dimensional mismatch, and the need for additional surgical interventions.[3] Moreover, the curative effect of this procedure is unsatisfactory as it offers partial functional recovery.[4] Thus, a synthetic device known as a nerve guidance conduit (NGC) has emerged as a promising alternative for facilitating peripheral nerve regeneration.

Regarding NGC manufacturing, three fundamental aspects must be addressed: material selection, structural design, and fabrication method. Naturally derived materials such as alginate, chitosan, collagen, gelatin, and silk have been used to fabricate NGCs because of their exceptional biocompatibility and biodegradability.[5–7] The commercially available NGCs composed of chitosan (Reaxon®) and collagen (NeuraGen®, Neuroflex®, NeuroMatrix®, RevolNerv®) have exhibited favorable outcomes in clinical trials; however, their use is limited in terms of mechanical strength and manipulability.[8] Concerns are also associated with batch-to-batch variability and high costs of NGC production.[9] Moreover, these conduits generate suboptimal results as compared to autografts.[10] Alternatively, synthetic materials are gaining marked attention because of their excellent mechanical properties and constant batch performance. NGCs have been manufactured using an assortment of bioresorbable synthetic polymers, including polylactic acid

[a] *Department of Paediatric Surgery, The Children's Hospital, Zhejiang University School of Medicine, National Clinical Research Center for Child Health, Hangzhou 310052, China. E-mail: shuqiang@zju.edu.cn*
[b] *State Key Laboratory of Fluid Power and Mechatronic Systems, School of Mechanical Engineering, Zhejiang University, Hangzhou 310027, China*

† Electronic supplementary information (ESI) available. See DOI: https://doi.org/10.1039/d4ma00073k

‡ These authors contributed equally to the work.

(PLA), poly(lactic-*co*-glycolic acid) (PLGA), polyglycolide acid (PGA), and polycaprolactone (PCL).[11] PCL extends among its counterparts as the most promising candidate for NGCs because of its cost-effectiveness in processing, ease of fabrication, and adjustable properties.[12] Currently, a commercially available NGC (Neurolac®) is composed completely of PCL. Several clinical trials have demonstrated that Neurolac® produces outcomes comparable to those of nerve autografts for defects of <3 cm. However, a notable shortcoming of this conduit lies in its simple structural design;[13] this single-channel conduit cannot accurately replicate the anisotropic architecture of native nerves and consequently impedes nerve function recovery.[14]

Commercial NGCs currently lack sophisticated structures to potentially improve microstructural guidance because of the limitation of fabrication methods, such as extrusion or injection molding techniques. These fabrication methods cannot typically produce the delicate features required for clinically relevant-sized devices and restrict the inclusion of micrometer-scale structural characteristics into the intra-luminal space.[15] Conduits with a multichannel structure have exhibited substantial advancements in controlling axonal dispersion and guiding directional reinnervation, thereby demonstrating improved efficiency.[16] Given these findings and the biomimetic organization of peripheral nerves, scalable fabrication methods that surpass traditional injection or extrusion processes must be urgently developed to produce biocompatible NGCs with a micrometer resolution.

Projection-based 3D printing (PBP) is an additive manufacturing method in which devices with intricate internal structures can be produced by solidifying the liquid precursor through a photochemical reaction.[17] PBP combined with a movable stage allows the precise control of the irradiation region and facilitates the fabrication of macroscopic-scale objects. This technique offers major advantages in fabricating scaffolds and devices with intricate microstructures by using a precursor under the CAD/CAM control.[18] Moreover, it may be scaled up efficiently to achieve mass production through the optimization of processing conditions, which enables automated and simultaneous object production on the same setup.[19] This technique is, however, currently restricted to a range of biocompatible materials. Nevertheless, it is used in the biomaterial molding process, and its ability to directly cure structures within a liquid precursor considerably simplifies the fabrication process.[20]

To synthesize poly(caprolactone) methacrylate (PCLMA), double bonds are incorporated at the termini of three-arm PCL molecules through a reaction between PCL and methyl methacrylate, which then imparts the photocuring group to the material.[21] This study employed the PBP method to precisely fabricate a series of 1-, 4-, and 7-channel NGCs by using a PCLMA precursor, aimed at peripheral nerve repair. The morphology of the fabricated NGCs was evaluated through optical microscopy and scanning electron microscopy (SEM). The mechanical properties of the prepared NGCs were assessed by conducting mechanical tests and finite element simulations. The fabricated NGCs were subsequently evaluated *in vitro* by using nerve cell cultures (rat Schwann cells 96) and *in vivo* by using a 10-mm-gap repair model in Sprague-Dawley (SD) rats (Fig. 1). This study represents an upgrading of the fabrication method to manufacture readily available NGCs, along with the systematic evaluation of the prepared NGCs through both *in vitro* and *in vivo* studies.

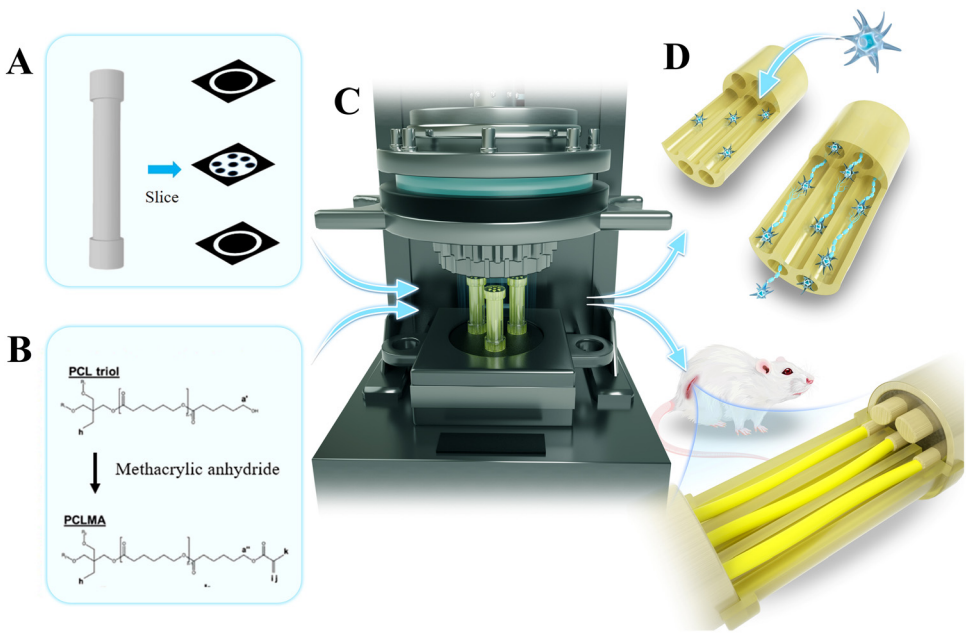

Fig. 1 Schematic illustration of the fabrication and biological performance evaluation of poly(caprolactone) methacrylate (PCLMA) nerve guidance conduits (NGCs). (A) Structural design of NGCs. (B) The synthetic process of PCLMA and preparation of photosensitive resin. (C) Fabrication of PCLMA NGCs *via* the projection-based 3D printing (PBP) method. (D) Biological performance evaluation of PCLMA NGCs *in vitro* and *in vivo*, respectively.

Material and methods

Formulation

PCLMA (EFL-PCLMA-3080), ethyl 2,4,6-trimethylbenzoylphosphonate (TPO-L, EFLOL), dichloromethane, and oil-soluble light absorbers (EFL-UVAO-001) were procured from Yongqinquan Intelligent Equipment Co., Ltd (Suzhou, China). First, 20 mg of oil-soluble light absorbers were dissolved in 1 mL of dichloromethane to prepare a standard photoabsorber solution. The prepolymer was then prepared by mixing 10 mL PCLMA solution with 50 mg photoinitiator TPO-L. The mixed solution was supplemented with 125 μL of the standard photoabsorber solution, followed by incubation at 50 °C for 30 min.

Photo-rheology of the PCLMA precursor

Photo-rheology of the PCLMA precursor was determined using a rheometer (MCR102, Austria) fitted with a plate/plate detection system. The bottom of a quartz plate was irradiated with a lamp source having a 405 nm wavelength and 13 mW cm^{-2} light intensity. The tests were conducted under varying temperatures (range: 40 °C–60 °C with a 5 °C interval) in the oscillation mode while maintaining the other parameters as follows: truncation gap, 100 μm; angular frequency, 1 rad s^{-1}; and strain amplitude, 1%. The storage modulus (G') and loss modulus (G'') were monitored for the initial 38 s, followed by subsequent light irradiation. Viscosities of the PCLMA precursor were measured during cooling and heating, spanning a temperature range from 35 °C to 65 °C, while maintaining the other parameters consistent with those of the photo-rheological measurement.

Design and fabrication of PCLMA NGCs using PBP

First, the stereolithography file format was created for the 1-, 4-, and 7-channel NGCs, which was subsequently used to fabricate the desired 3D object by employing a commercial PBP system (EFL-BP8601Pro, Yongqinquan Intelligent Equipment Co., Ltd, Suzhou, China). The detailed procedures are described in our previous studies.[22,23]

The outer diameter of the conduit was 2.0 mm, while the inner diameters of the 1-, 4-, and 7-channel conduits were 1.5 mm, 500 μm, and 400 μm, respectively. Conduits with two heights were fabricated: (1) 2-mm-high conduits for the RSC96 culture for *in vitro* evaluation and (2) 10-mm-high conduits for mechanical testing, *in vivo* implantation, and *in vivo* evaluation. To allow the suturing of a nerve stump *in vivo*, a specially designed capped portion was incorporated on both sides. The capped portion had a diameter and length of 2.5 and 2.0 mm, respectively. Based on the preliminary trial results, the printing parameters were established as follows: vat temperature, 50 °C; printing platform temperature, 37 °C; light intensity, 13 mW cm^{-2}; and printing thickness, 50 μm. The exposure time of NGCs for the *in vitro* evaluation was 3 s, and those for the *in vivo* evaluation were 13, 13, and 8.5 s for 1-, 4-, and 7-channels, respectively. To exclude the residual uncured polymer, the printed NGCs were thoroughly rinsed with 1 : 1 methanol/isopropanol.

Characterization of PCLMA NGCs

The morphological characteristics of the PCLMA NGCs were analyzed by visualizing the samples under an optical microscope (BX51, Olympus, Japan) and a scanning electron microscope (JSM-IT100, Japan). After a longitudinal incision was made, the samples were treated using a gold-sprayed apparatus. SEM was performed to visualize and analyze the microscopic morphology of the fabricated NGCs.

Mechanical properties of the PCLMA NGCs were evaluated using a universal testing machine (UTM2102, China), with the samples subjected to a compression deformation rate of 2 mm min^{-1} until failure. The force–displacement, and stress–strain curves were graphically illustrated. Compressive strength was determined using the normalized area approach. Geometric parameters of the conduits, including their channel numbers, diameters, cross-sectional areas, volumes, inner surface areas, and surface area-to-volume ratios, were calculated. The compressive force for NGCs with different channels was simulated using a finite element model, which was established using the Ansys Workbench software (ANSYS19, USA). The finite element model with consistent parameters was used to conduct compression simulation experiments, which were in agreement with actual mechanical testing. After the bottom of the conduit was secured, a uniform force was applied from the top to evaluate its strength under the actual test.

PCLMA discs (2 mm height, 4 mm diameter) were prepared by injection syringe with 13 mW cm^{-2} light intensity for 3 s. Commercial PCL(M_n 80 000 Da) was set as the control group. The PCLMA discs and same-sized discs of PCL were placed in phosphate-buffered saline (PBS, 1×) and 5 M NaOH in an incubator at 37 °C. After they were removed from the solvent and dried under a vacuum for 1 d, the degradation rates of samples were determined gravimetrically at time points of 5–21 days. The degradation rates were calculated with the percentage of remaining weight to initial weight.

***In vitro* RSC96 culture.** RSC96 was employed to investigate the cytocompatibility of PCLMA NGCs. The cells were cultured in Dulbecco's Modified Eagle's Medium (Gibco, USA) supplemented with 10% fetal bovine serum (Gibco, USA) and penicillin–streptomycin (Gibco, USA) under standard conditions (5% CO_2, 37 °C) in an incubator. Before the cells were seeded, the PCLMA samples were immersed in 75% ethanol and exposed to ultraviolet light for 2 h for sterilization. After the samples were washed with PBS three times, 50 μL of the RSC96 suspension (5×10^4 cells per mL) was loaded onto the samples in a 12-well tissue culture plate. The plates were transferred into an incubator for 2 h for cell attachment. Subsequently, the RSC96 cell-laden PCLMA NGCs were incubated with a 2 mL fresh culture medium. After 1, 2, and 3 days of culture in the medium, cell proliferation on PCLMA NGCs with different channels was evaluated using the cell counting kit (CCK-8, Beyotime, China) according to the manufacturer's specifications. The tissue culture polystyrene (TCP) was established as the control group. The cell proliferation rate at different time points was determined by calculating the ratio of the CCK-8 value on each day to that measured on the initial day. After 1 day

of cultivation, cell viability was assessed through live–dead staining. The RSC96 cell-laden PCLMA NGCs were incubated for 15 min in the staining working solution containing 2 mM of calcein AM and 6 mM of propidium iodide (Beyotime, China). The images were captured using a laser-scanning confocal fluorescence microscope (FV1200, Olympus, Japan). Cell viability was evaluated by quantifying the number of stained cells. For cytoskeleton staining, the laden PCLMA NGCs were cultured for 7 days and fixed in 4% paraformaldehyde for 30 min. Subsequently, they were permeabilized in 0.25% Triton X-100 (Gibco, USA) for 15 min and blocked with 2% bovine serum albumin (BSA, Gibco, USA) for 10 min at room temperature. The samples were further stained with the actin-tracker green fluorescent probe (Beyotime, China) for 45 min. The cell nuclei were stained with 4′,6-diamidino-2-phenylindole (DAPI) (Beyotime, China) for 10 min, and the cells were observed under the laser-scanning confocal fluorescence microscope.

Surgical procedures

The nerve defect model was established to investigate the *in vivo* nerve regeneration capability of NGCs. Before animal surgery, all implantable NGC samples were immersed in 75% ethanol and exposed to ultraviolet light for 2 h for sterilization and then rinsed three times with PBS. All animal experiments were ethically approved by the ethics committee of Zhejiang University. In total, 24 male adult SD rats (average weight: approximately 200–220 g) were randomly and equally divided into four experimental groups (Autograft, 1-channel, 4-channel, and 7-channel groups). Before the surgery, the rats were intraperitoneally anesthetized by injecting 1% sodium pentobarbital at 40 mg kg^{-1} body weight. The right sciatic nerve was exposed by making an incision from the distal thigh to the sciatic notch. A 10-mm segment was excised to create a deliberate gap (Fig. S1, ESI†). Both sides of the nerve stump were inserted 2 mm into the capped portion of the NGCs and firmly secured using an 8-0 monofilament nylon suture. In the Autograft group, the excised nerve segment was sutured in a reversed orientation. After the surgical site was cleansed and sterilized, the muscular and cutaneous layers were meticulously sutured using a 5–0 nylon suture.

Gait analysis

Gait analysis was performed to assess the motor function after 6 and 12 weeks of implantation. The experimental feet were immersed in ink, and the animals were positioned in a custom-made box (length: 80 cm; width: 10 cm). To calculate the sciatic function index (SFI), at least five distinct footprints of the experimental legs (E) and normal legs (N) were required. SFI was calculated as follows:

$$\mathrm{SFI} = -38.3(\mathrm{EPL\text{-}NPL})/\mathrm{NPL} + 109.5(\mathrm{ETS\text{-}NTS})/\mathrm{NTS} + 13.3(\mathrm{EIT\text{-}NIT}) - 8.8$$

where PL, TS and IT denote paw length, toe spread length, and intermediary toe spread length, respectively.

Electrophysiological analysis

Electromyography (Dentec, Holland) was performed for electrophysiological analysis after 12 weeks of implantation. Following the administration of anesthesia, the sciatic nerve was exposed through the previous surgical approach. Four pins were inserted, with the stimulating pin positioned close to the graft, and the recording pin was placed at the gastrocnemius muscle. The reference pin was positioned between the stimulating and receiving pins, and the ground pin was situated at the mouse's tail. Identical stimuli (stimulus intensity = 6 mA, frequency = 1 Hz, duration = 1 ms) were applied at the proximal and distal grafts. The compound muscle action potential (CMAP) amplitude and latency were recorded, and the nerve conduction velocity (NCV) was calculated.

Histological analysis of regenerated nerves

After the electrophysiological analysis was completed, all animals were promptly euthanized. The specimens harvested from the middle segments were fixed with 4% paraformaldehyde. Following dehydration, paraffin was used to embed the tissue. Longitudinal sections (thickness: 5 μm) were stained with hematoxylin and eosin (H&E) and toluidine blue. Then, the sections were examined under an optical microscope.

Immunohistochemistry analysis

For immunofluorescence detection at the cellular level, sections of the middle segments of the specimens were stained with NF-200 (1:100, Abcam, USA) and S-100 (1:200, Abcam, USA). To block nonspecific antigens, 1% BSA was used to incubate the specimens. The sections were mixed with the primary antibody overnight at 4 °C, washed with PBS, and incubated with a combination of fluorescein isothiocyanate (FITC)-labeled secondary antibodies (1 : 200, Invitrogen, USA) for 2 h at normal atmospheric temperature. Cell nuclei were incubated with DAPI. The stained specimens were examined under a laser-scanning confocal microscope. The positive NF-200 and S-100 staining areas of the regenerated nerves were quantified using Image-Pro Plus software for image analysis.

Gastrocnemius muscle analysis

At 12 weeks after implantation, the gastrocnemius muscles of the operated hind limbs were collected and fixed using 4% paraformaldehyde overnight at 4 °C. Transverse sections of the muscles embedded in paraffin wax were obtained using a microtome for histological staining with hematoxylin and eosin (H&E) and Masson's trichrome. To measure the diameter and area of muscle fibers and the percentage of collagen fibers, five images were randomly captured from each H&E- and Masson's trichrome-stained section and analyzed using Image-Pro Plus software.

Statistical analysis

The experimental data were presented as mean ± standard deviation. Statistical analyses were conducted using analysis of variance. The single (*) and double (**) asterisks indicated a

statistically significant difference at $P < 0.05$ and $P < 0.01$, respectively. NS denoted no statistical difference with $P > 0.05$.

Results and discussion

Photorheological properties of PCLMA

The photorheological properties of PCLMA must be evaluated before the PBP procedure.[24] The temperature at which the material is applied considerably influences the printing outcome of the scaffold. Print defects and potential failures resulting from inappropriate viscosity are attributable to unsuitable temperatures.[25] Therefore, the viscosity of PCLMA must be evaluated at different temperatures. Under constant temperature conditions, the viscosity consistently maintained stability (Fig. 2(A)). Furthermore, regardless of whether the heating or cooling mode was employed, viscosity declined with an increase in temperature (Fig. 2(B)).

To characterize the photocuring process, the polyreaction of PLCMA was monitored at different temperatures. Under identical conditions (wavelength = 405 nm, light intensity = 13 mW cm^{-2}), similar reaction patterns were observed (Fig. 2(C)). Before illumination, the storage modulus (G') and loss modulus (G'') of PLCMA remained almost constant, which indicated a sol state. At this stage, G'' was greater than G'. Both G' and G'' increased rapidly after exposure to light. Once photopolymerization was completed, G' became larger than G'', signifying a transformation from the liquid state to the solid state. These results suggest that PCLMA has sufficiently low viscosity and excellent photocuring properties and thus it meets the material requirement for PBP applications.

Fabrication and morphology of PCLMA NGCs

The establishment of appropriate printing parameters, including light intensity, height, and exposure time during the PBP procedure, is a prerequisite for fabrication.[26] First, 1- and 4-channel PCLMA NGCs were fabricated with a light intensity of 13 mW cm^{-2}, a height of 50 μm, and an exposure time of 13 s. The 7-channel PCLMA NGCs were obtained successfully by adjusting the exposure time to 8.5 s. If the desired structure cannot be achieved initially, the exposure time must be first altered as the primary parameter adjustment, followed by the modifications of height and light intensity. Additionally, post-processing in which an organic solvent is used for removing the residual uncrosslinked material is vital in ensuring that the channels are unobstructed and should not be ignored.[27] To optimize the printing procedure, a protocol was developed to enhance production efficiency by setting multiple images on the digital micromirror device (DMD). Accordingly, five structures could be simultaneously fabricated. The entire fabrication process, including modeling, parameter setting, polymerization, and post-processing, was completed in approximately 5 min. This corresponds to a production rate of one structure per minute. This emphasizes a significant advantage of PBP as a fabrication method. PBP has the potential for rapid and scalable production following the construction of the equipment and its calibration, along with that of the processing conditions. Additionally, conduit dimensions could be adjusted flexibly by modifying the cross-sectional dimensions of the structure and uploading images onto the DMD, with no additional modification required to the setup.

Following parameter optimization and post-processing, the PCLMA NGCs with different channels were prepared, ensuring formation stability and convenient intraoperative handling. Fig. 3(A) and (B) display the longitudinal and transverse views of the conduits with 1-, 4-, and 7-channels, respectively. Geometric parameters of NGCs were designed to simulate the natural architecture of the rat sciatic nerve (Table 1). The physiological dimensions of the epineurium ranged from 1.5 to 2 mm in diameter, while those of the endoneurium ranged from 400 to 500 μm in diameter.[28] The conduit had a total length of 14 mm, with a 2-mm capped portion on both ends to bridge a 10-mm nerve injury gap. The capped portion could be inserted into the severed nerve end, which offered considerable convenience for suturing. The fabricated 1-channel NGCs had an inner diameter of 1.47 ± 0.03 mm and a wall thickness of 250 μm, respectively (Fig. S2, ESI†). The inner diameter of 1-channel NGCs was close to the physiological dimension of the rat sciatic nerve (1.5–2 mm). The fabricated 4- and 7-channel NGCs had inner diameters of 500 ± 50 μm and 400 ± 40 μm, respectively (Fig. S2 and S3, ESI†). The inner diameters of 4-channel and 7-channel NGCs were comparable to the dimensions of the endoneurial structure of the native rat sciatic nerve (400–500 μm). From a biomimetic perspective, the 1-channel

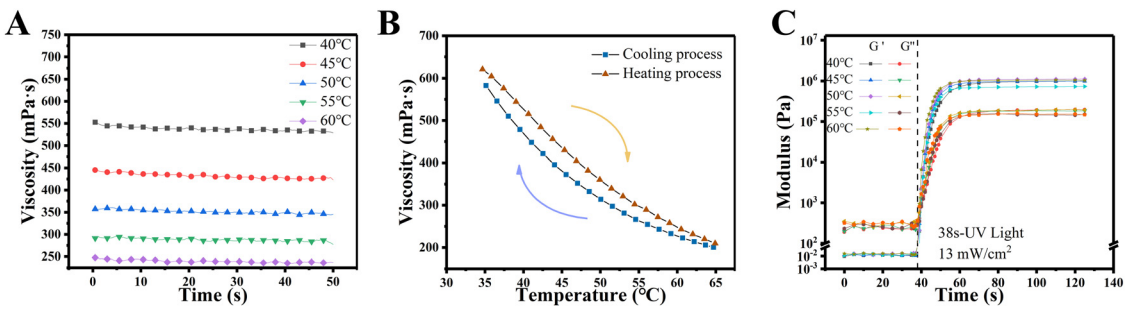

Fig. 2 Photorheological properties of PCLMA. (A) Viscosity-time plot of PCLMA. (B) Viscosity-temperature plot of PCLMA in cooling and heating process. (C) Storage and loss modulus-time plots of PCLMA, light irradiation started after 38 s.

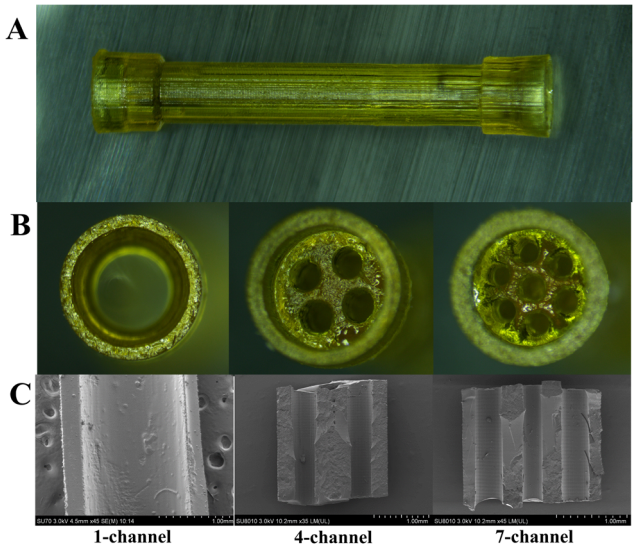

Fig. 3 Morphological characteristics of PCLMA NGCs. (A) Optical microscope images (1×) showing the longitudinal view (the dotted yellow line of the image on the right shows the plane where the samples were cut to acquire longitudinal images). (B) Optical microscope images (2×) showing the transverse view. (C) Scanning electron microscopy images showing the longitudinal section.

and multichannel replicated the inner and outer membrane structures of the native nerve, respectively. Additionally, the SEM images showed that all longitudinal channels were accurately arranged and completely unobstructed (Fig. 3(C)).

Mechanical and degradation properties of PCLMA NGCs

The mechanical properties of the NGCs have a vital effect on the microenvironment for nerve regeneration. Fig. 4(A) and (B) show that the force–displacement, and stress–strain curves were close to the linear behavior. The compressive strengths of 1-, 4-, and 7-channel PCLMA NGCs were 689.2, 3057.2, and 979.4 KPa, respectively (Fig. 4(C)). The lowest compressive strength was noted for the 1-channel NGCs. The mechanical strength of 1- and 7-channel PCLMA NGCs is comparable to that of native nerves (0.5–13 MPa), while the strength of the 4-channel exceeds that of native nerves.[22] The geometric parameters of NGCs were calculated (Table 1). The compressive strength was determined on the basis of the cross-sectional area, rather than the number of channels. The 4-channel NGCs had a minimum cross-sectional channel, which meant that they had the largest force area. Thus, the highest compressive strength was observed for the 4-channel NGCs, which was 4.4-fold higher than that of the 1-channel NGCs. The compressive strength of the 7-channel NGCs was 1.4-fold higher than that of the 1-channel NGCs. In the case of multichannel (4-, and 7-channel) NGCs, the higher compressive strength was possibly attributable to their more solid structure than that of the 1-channel NGCs. Based on the finite element analysis, we further evaluated the mechanical strength of the NGCs (Fig. 4(D)). In the finite element model, the compressive strengths of the 1-, 4-, and 7-channel PCLMA NGCs were 4.53, 22.52, and 12.23 MPa, respectively. Although the simulated compressive strength was larger than the actual compressive strength, they still exhibited a similar trend. Notably, the compressive strength of the PCLMA NGCs can be adjusted flexibly by modifying the channel number and diameter of the conduit.

The polymer degradation rate is an important characteristic of NGCs that should match the time required for nerve regeneration. The degradation of PCLMA was slow, with 97.5 ± 0.9% remaining after 21 days in PBS, as depicted in Fig. 5(E) and (F). This result was comparable to that of the commercial PCL (98.7 ± 0.4%). In an alkaline solution, both PCLMA and PCL exhibited faster degradation rates of 90.5 ± 0.6% and 93.2 ± 0.2%, respectively, due to the accelerated hydrolysis reaction.[21] The enhanced degradation rate of PCLMA, in comparison to the linear PCL, is of particular interest for nerve regeneration due to the prolonged presence of the linear PCL *in vivo* for over three years.[29] The extended placement of NGC within the body may result in chronic foreign body reaction and fibrous encapsulation. A faster degradation rate of PCLMA is desired, which can be adjusted by changing the degree of methacrylation.[30]

Biocompatibility of PCLMA NGCs *in vitro*

The biocompatibility of the conduit materials is essential for nerve tissue regeneration. Therefore, the biological behavior of the PCLMA NGCs was confirmed by investigating the cell–material interaction through the culturing of RSC96 on the PCLMA NGCs. The fabricated PCLMA NGCs were designed to have a 2-mm height to facilitate *in vitro* investigations on the cell–material interaction. After 1 day of cell cultivation, cell viability was assessed in the live–dead cell staining assay. The PCLMA NGCs with 1-, 4-, and 7-channels exhibited average cell viabilities of 96.3%, 96.9%, and 97.9%, respectively, which were close to 100% and demonstrated no statistically significant differences among the groups ($P > 0.05$, Fig. 5(A)). Cell proliferation on PCLMA NGCs at 1, 2, and 3 days was evaluated through the CCK-8 assay. The OD_{450} value can serve as an indicator of the RSC96 count. Cell proliferation occurred in all experimental groups over time (Fig. 5(B)). At three specific time points, the OD_{450} values of the PCLMA NGCs with different channels were comparable ($P > 0.05$) and exhibited no significant difference as compared with those of the TCP ($p > 0.05$).

Table 1 Geometrical parameters of different channel PCLMA NGCs

Samples	Outer diameter (mm)	Inner diameter (mm)	Cross-sectional area (mm^2)	Inner surface area (mm^2)	Volume (mm^3)	Inner surface area to volume ratio (mm^{-1})
1-Channel	2.0	1.5	1.77	47.10	17.70	2.66
4-Channel	2.0	0.5	0.78	62.80	7.80	8.05
7-Channel	2.0	0.4	0.88	87.92	8.80	9.99

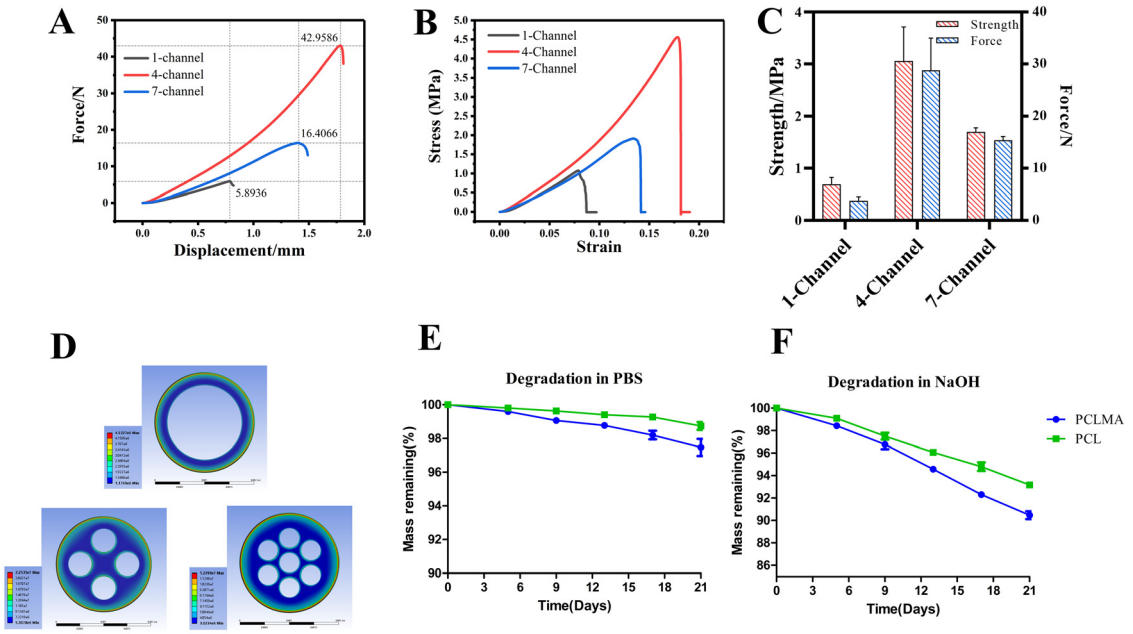

Fig. 4 Mechanical and degradation properties of PCLMA NGCs. (A) Compressive force–displacement curves. (B) Compressive stress–strain curves. (C) Compressive strength and force of PCLMA NGCs. (D) Finite element analysis of 1-,4- and 7-channel PCLMA NGCs. (E) Degradation in PBS. (F) Degradation in NaOH.

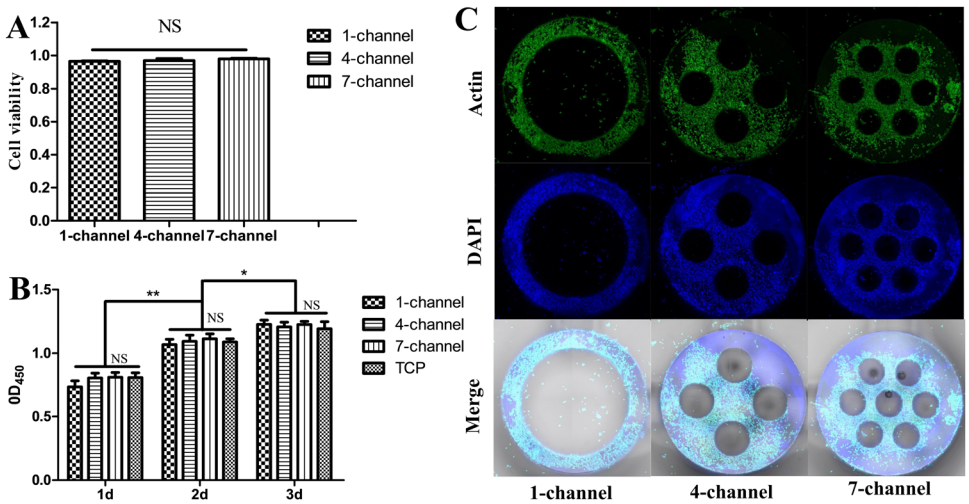

Fig. 5 Biocompatibility of PCLMA NGCs *in vitro*. (A) Cell viability of RSC 96 cells after culturing for 1 d. (B) The proliferation of RSC 96 cells after culturing for 1, 2, 3 d. (C) The distribution and spread of RSC 96 cells on PCLMA NGCs after culturing for 7 d.

The distribution of RSC96 on PCLMA NGCs was examined through cell cytoskeleton staining at 7 days of cell cultivation. Fig. 5(C) demonstrates that the cells were homogeneously distributed on the PCLMA, along with an elongated morphology of the cytoskeleton. Collectively, these findings indicate that PCLMA NGCs are non-cytotoxic and promote neuronal cell survival, adhesion, and proliferation (Fig. S5, ESI†).

Walking track analysis

The sciatic nerve extends into the common peroneal nerve and tibial nerve in the popliteal fossa, which governs foot sensation and movement. Motor functions must be re-established to achieve practical functional recovery after nerve injury. SFI, a non-invasive modality, can be used for evaluating the extent of functional recovery.[31] The maximum and minimum values of SFI were 0 and −100, which indicated normal function and complete impairment, respectively. The SFI magnitude reflects the severity of sciatic nerve dysfunction. The initial SFI was not significantly different among the four groups after 6 weeks of implantation ($P > 0.05$, Fig. 6(A)). The SFI value increased progressively throughout the experiment, which indicates the sustained progression of the repair process. After 12 weeks of

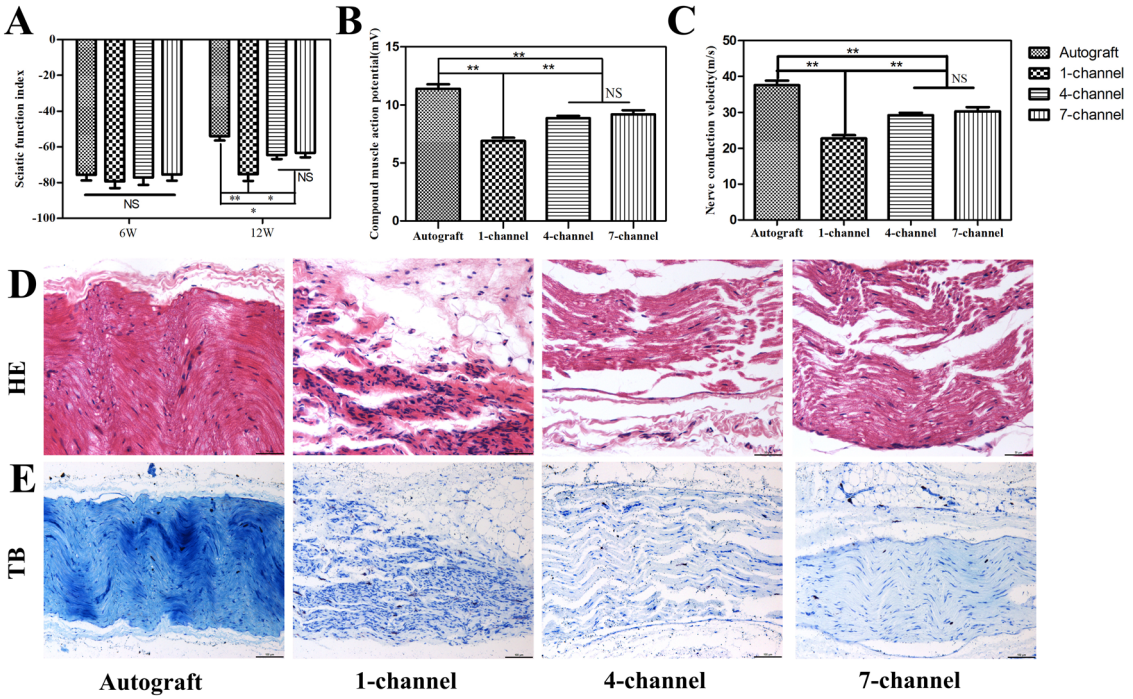

Fig. 6 The evaluation of functional recovery, electrophysiology, and regenerated nerves by H&E and toluidine blue staining. (A) Quantitative analysis of SFI calculated by gait analysis after 6 and 12 weeks of implantation. (B) and (C) (Quantitative analysis of functional regeneration by measuring NCV) (B), and CMAP (C), after 12 weeks of implantation. (D) and (E) Histological examination of the regenerated nerve tissue by H&E staining (D) and toluidine blue staining (E) after 12 weeks of implantation.

implantation, the autograft, 4-, and 7-channel groups exhibited significant improvements as compared with the 1-channel group. The autograft group (-53.93 ± 5.55; $P < 0.05$) exhibited a significantly higher SFI value than the multichannel groups. The autologous nerve graft is widely recognized as the gold standard for the clinical repair of nerve defects.[32] The closer the repair ability approaches of the conduits were to those of the autologous nerve graft, the more effective the conduits became in facilitating successful repair. Currently, few tissue engineering scaffold repair approaches are available that exhibit an efficacy comparable to that of the autologous nerve graft.[33] According to studies, the SFI values of the conduit groups exhibit a lower trend than those of the autograft group after 8 weeks of implantation, with some values remaining lower even after 16 weeks of implantation.[34,35] Consequently, achieving SFI values equivalent to or even superior to those of the autologous nerve graft may necessitate an extended duration for repair. The SFI values for the 4- and 7-channel groups were -64.50 ± 5.16 and -63.27 ± 5.73, respectively, and exhibited no statistically significant difference ($P > 0.05$). The multichannel groups had significantly higher SFI values than the 1-channel group (-75.30 ± 6.40). This manifests that contradictory to the 1-channel conduit, the multichannel structure can prompt nerve regeneration and improve the functionality of the innervated tissue.

Electrophysiology

Sciatic nerve regeneration can be effectively evaluated through electrophysiological testing. The regenerated nerve fibers must establish connections with the distal target muscle across the nerve defect gap to form the CMAP. The CMAP amplitude can indicate nerve regeneration, while NCV reflects the speed at which these regenerated nerves transmit signals.[36] CMAP and NCV of the regenerated nerves in all experimental groups are presented in Fig. 6(B) and (C). After 12 weeks of implantation, maximum CMAP and NCV values were noted for the autograft group (11.37 ± 0.87 mV, 37.45 ± 2.87 m s^{-1}, respectively). The 4-channel (8.87 ± 0.46 mV, 29.27 ± 1.50 m s^{-1}) and 7-channel groups (9.20 ± 0.80 mV, 30.35 ± 2.64 m s^{-1}) displayed non-significant differences ($P > 0.05$) in the CMAP and NCV values, but these values were significantly higher than those of the 1-channel group (6.9 ± 0.61 mV, 22.77 ± 2.02 m s^{-1}, respectively; $P < 0.05$). The CMAP and NCV values exhibited a consistent tendency toward SFI. These findings provide further evidence that a multichannel conduit yields higher efficacy in promoting nerve function recovery than a single-channel conduit.

Histological assessment of regenerated nerves

To evaluate any histological improvement in the regenerated nerve, staining techniques, including H&E and toluidine blue staining, were performed after 12 weeks of implantation. Regenerating nerve fibers emanated from the proximal stump and infiltrated the conduit, ultimately coalescing into a bundled architecture (Fig. 6(D) and (E)). The new nerve tissues were well organized and exhibited a clear alignment along the longitudinal axis of the conduit, guided by the aligned fibers present in both 4- and 7-channel groups. However, the regrown axons in the 4- and 7-channel groups were denser than those in

the 1-channel group. Geometric parameters can affect the process of directing peripheral nerve regeneration. These parameters play a pivotal role in topographic guidance cues. According to multiple studies, the ISA/V of the channels inside the NGCs can effectively reflect the impact of the channel diameter, cross-sectional area, and surface area on nerve repair.[36–39] The obtained results convincingly prove that a higher ISA/V can result in greater efficacy in promoting nerve regeneration. A high ISA/V is speculated to create an optimal microenvironment for biological components such as growth factors, enzymes, and nucleic acids. It also enhances efficient cell implantation and proliferation, thereby facilitating the spatial distribution and nutrient exchange of cells.[40]

Immunofluorescence analysis of regenerated nerves

In peripheral nerve regeneration, Schwann cells (SCs) play a pivotal role as they undergo differentiation and offer guidance cues to the regenerating axon to reconnect across the nerve gap after injury.[41] To evaluate nerve regeneration at the cellular level, immunofluorescence staining of NF-200 and S-100 in regenerated nerves was performed after 12 weeks of implantation. During immunofluorescence staining, the cell nucleus, S-100 protein, and NF-200 protein were stained blue, red, and green, respectively. Both NF-200 and S-100 proteins were determined in all experimental groups, providing evidence for the ingrowth of newly formed axons and the development of myelin sheaths composed of SCs (Fig. 7(A)). Fig. 7(B) and (C) display that the positive area percentages of both NF-200 and S-100 were the highest in the autograft group. The expression levels of both markers in the multichannel groups were markedly higher as compared to the 1-channel group ($P < 0.01$). The expression level was slightly higher in the 7-channel group than in the 4-channel group but no significant differences were detected ($P > 0.05$). The results demonstrated that the multichannel conduits had a significantly higher density of SCs and promoted enhanced remyelination as compared with the 1-channel conduit, thereby providing further evidence for supporting axonal regeneration.

Histological assessment of gastrocnemius muscle

The gastrocnemius muscle is a crucial player in lower limb function. In patients with sciatic nerve damage, disuse atrophy may occur in the gastrocnemius muscle, which is characterized by weight loss, reduced muscle belly size, decreased muscle cell volume, and increased collagen deposition.[42] Reconstruction of the sciatic nerve structure leads to the reorganization of innervated muscles, which further results in partial and varying degrees of reversibility or restoration. Consequently, neurological function restoration can be indirectly observed through changes in innervated muscles.[43] After 12 weeks of implantation, H&E and Masson's trichrome staining of the gastrocnemius muscle revealed the muscle fiber morphology in all experimental groups. Evident signs of muscle atrophy and collagen deposition were noted, specifically in the 1-channel NGCs (Fig. 8(A) and (B)). The autograft group demonstrated the highest average diameter and area of muscle fibers. No significant difference in the average diameter and area of muscle fibers was observed between the 4- and 7-channel groups ($P > 0.05$). However, their values were greater than those of the 1-channel group (Fig. 8(C) and (D), $P < 0.01$). The muscle fibers were stained red, while the collagen was stained blue during Masson's trichrome staining. The morphometric analysis of Masson's trichrome staining unveiled a trend consistent with that of H&E staining across all experimental groups (Fig. 8(E)). The collagen content in the 4- and 7-channel groups was

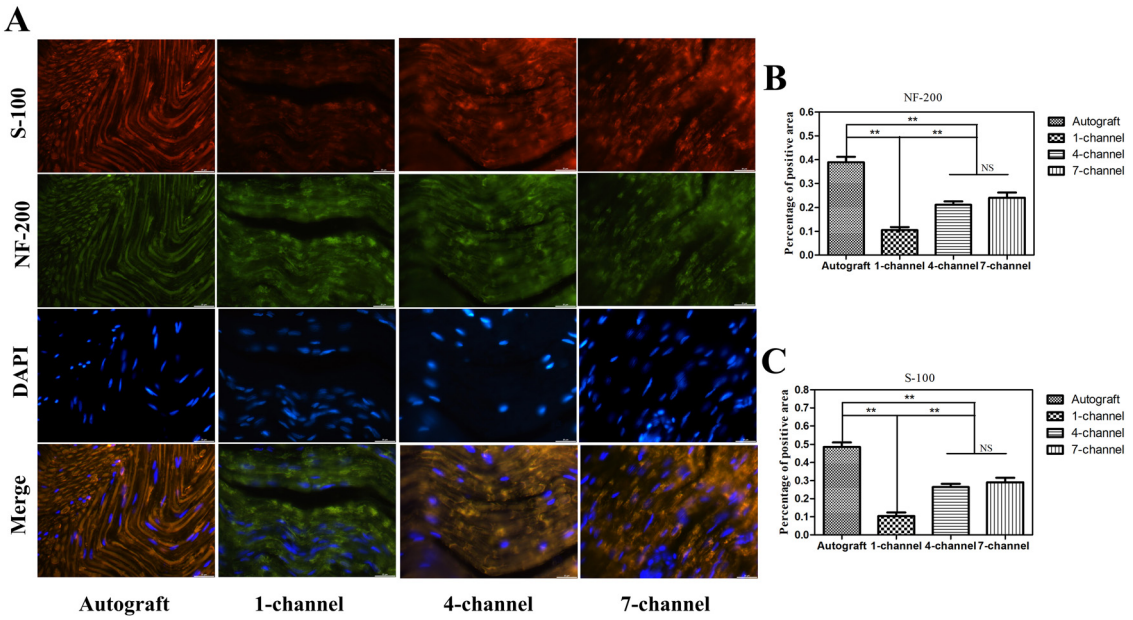

Fig. 7 Immunofluorescence analysis of regenerated nerves after 12 weeks of implantation. (A) Immunofluorescence staining of NF200 (green), S-100 (red), DAPI (blue), and merging of the regenerated nerves. (B) Percentage of the NF-200 positive area. (C) Percentage of the S-100 positive area.

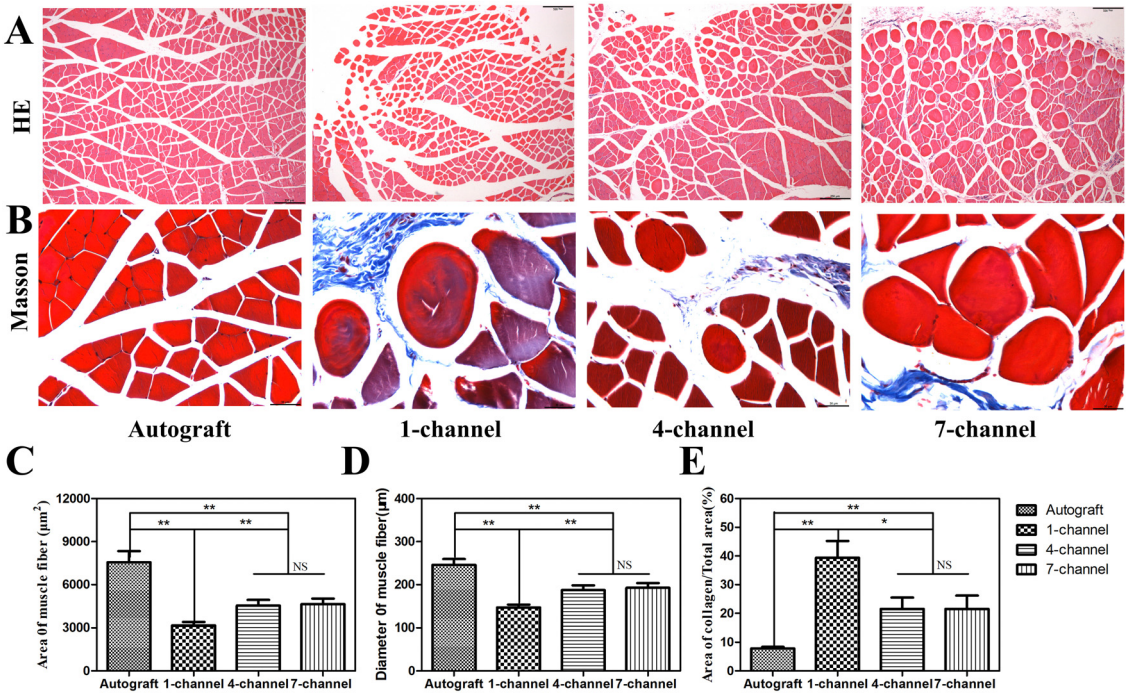

Fig. 8 Histological assessment of the gastrocnemius muscle in all experimental groups after 12 weeks of implantation. (A) and (B) Histological examination of the gastrocnemius muscle by H&E staining (A) and Masson's trichrome staining (B). (C) Area of muscle fiber. (D) Diameter of muscle fiber. (E) Area of collagen/Total area.

significantly lower than that in the 1-channel group ($P < 0.05$), which, however, was notably higher than that in the autograft group ($P < 0.01$). The longitudinally arranged channels within the multichannel conduit present large surface areas for SC attachment and growth factor delivery, while also limiting axonal dispersion, compared with the single channels of the 1-channel conduit.[44] Therefore, multichannel conduits contribute to boosting gastrocnemius muscle restoration with their excellent capacity.

Conclusion

We have presented the use of a PBP system capable of fabricating conduits for peripheral nerve regeneration. The material of choice, PCLMA, has low viscosity and rapid photocuring properties and thus satisfies the requirement of the PBP procedure. The PBP system can fabricate a series of PCLMA NGCs with 1-, 4-, and 7-channels with high fidelity. The PCLMA NGCs prepared herein promote neuronal cell survival, adhesion, and proliferation *in vitro*. Multichannel NGCs exhibited superior nerve regeneration capabilities as compared to 1-channel NGCs *in vivo*. Overall, this study highlights the potential of PBP to rapidly produce precise and intricate NGC structures, thereby enabling individual customization. Ongoing future developments include fabricating larger conduits and investigating longer implantation times by using larger injury gap models. This approach offers diverse advantages for manufacturing clinically relevant scaffolds.

Author contributions

Q. Shu supervised the research, designed the experiments and conceived the idea. H. Li, K. Yao and Y. Chen performed the experiments and analyzed the data. H. Li and K. Yao drafted the manuscript. W. Ye and Q. Shu revised the manuscript. All authors gave approval to the final version of the manuscript to be published.

Conflicts of interest

The authors declare no conflicts of interest.

Acknowledgements

This research was supported by the Zhejiang Province Nature Science Foundation of China under grant no. 23H090012.

References

1 H. Ying and J. Yin, *Biodes. Manuf.*, 2022, **5**, 6–8.
2 O. A. Selim, S. Lakhani, S. Midha, A. Mosahebi and D. M. Kalaskar, *Tissue Eng., Part B*, 2022, **28**, 295–335.
3 C. Raza, H. A. Riaz, R. Anjum and N. U. A. Shakeel, *Life Sci.*, 2020, **243**, 117308.
4 J. Zhang, J. Tao, H. Cheng, H. Liu, W. Wu, Y. Dong, X. Liu, M. Gou, S. Yang and J. Xu, *Burns. Trauma*, 2022, **10**, tkac010.
5 J. Rao, Y. Cheng, Y. Liu, Z. Ye, B. Zhan, D. Quan and Y. Xu, *Mater. Sci. Eng., C*, 2017, **73**, 319–332.

6 G. Ding, X. Li, M. Sun, Y. He, F. Zhao, T. Wu, J. Wang, S. Ren, W. Shi, L. Xu, X. Hu, W. Huang, R. Yu and Y. Ao, *Chem. Eng. J.*, 2022, **431**, 133861.
7 H. Gong, H. Fei, Q. Xu, M. Gou and H. H. Chen, *J. Biomed. Mater. Res., Part A*, 2020, **108**, 805–813.
8 K. Liu, L. Yan, R. Li, Z. Song, J. Ding, B. Liu and X. Chen, *Adv. Sci.*, 2022, **9**, e2103875.
9 Y. Zhu, D. Joralmon, W. Shan, Y. Chen, J. Rong, H. Zhao, S. Xiao and X. Li, *Biodes. Manuf.*, 2021, **4**, 405–428.
10 P. Meena, A. Kakkar, M. Kumar, N. Khatri, R. K. Nagar, A. Singh, P. Malhotra, M. Shukla, S. K. Saraswat, S. Srivastava, R. Datt and S. Pandey, *Cell Tissue Res.*, 2021, **383**, 617–644.
11 X. Zhang, W. Qu, D. Li, K. Shi, R. Li, Y. Han, E. Jin, J. Ding and X. Chen, *Adv. Mater. Interfaces*, 2020, **7**, 2000225.
12 J. R. Thompson, K. S. Worthington, B. J. Green, N. K. Mullin, C. Jiao, E. E. Kaalberg, L. A. Wiley, I. C. Han, S. R. Russell, E. H. Sohn, C. A. Guymon, R. F. Mullins, E. M. Stone and B. A. Tucker, *Acta Biomater.*, 2019, **94**, 204–218.
13 D. N. Rodríguez-Sánchez, G. B. A. Pinto, L. P. Cartarozzi, A. L. R. de Oliveira, A. L. C. Bovolato, M. de Carvalho, J. V. L. da Silva, J. A. Dernowsek, M. Golim, B. Barraviera, R. S. Ferreira, E. Deffune, M. Bertanha and R. M. Amorim, *Stem. Cell. Res. Ther.*, 2021, **12**, 303.
14 J. Wang, H. Xiong, T. Zhu, Y. Liu, H. Pan, C. Fan, X. Zhao and W. W. Lu, *ACS Nano*, 2020, **14**, 12579–12595.
15 K. M. Pawelec, C. Yoon, R. J. Giger and J. Sakamoto, *Biomaterials*, 2019, **216**, 119263.
16 T. Yu, L. Wen, J. He, Y. Xu, T. Li, W. Wang, Y. Ma, M. A. Ahmad, X. Tian, J. Fan, X. Wang, H. Hagiwara and Q. Ao, *Acta Biomater.*, 2020, **115**, 235–249.
17 J. Gong, Y. Qian, K. Lu, Z. Zhu, L. Siow, C. Zhang, S. Zhou, T. Gu, J. Yin, M. Yu, H. Wang and H. Yang, *Biomed. Mater.*, 2022, **17**, 2004.
18 P. Song, M. Li, B. Zhang, X. Gui, Y. Han, L. Wang, W. Zhou, L. Guo, Z. Zhang, Z. Li, C. Zhou, Y. Fan and X. Zhang, *Composites, Part B*, 2022, **244**, 110163.
19 S. Peng, Y. Li, L. Wu, J. Zhong, Z. Weng, L. Zheng, Z. Yang and J. T. Miao, *ACS Appl. Mater. Interfaces*, 2020, **12**, 6479–6488.
20 N. A. Traugutt, D. Mistry, C. Luo, K. Yu, Q. Ge and C. M. Yakacki, *Adv. Mater.*, 2020, **32**, e2000797.
21 J. Field, J. W. Haycock and F. M. Boissonade, *Molecules*, 2021, **26**, 1199.
22 H. Li, K. Yu, P. Zhang, Y. Ye and Q. Shu, *J. Biomater. Appl.*, 2022, **37**, 538–550.
23 W. Ye, H. Li, K. Yu, C. Xie, P. Wang, Y. Zheng, P. Zhang, J. Xiu, Y. Yang, F. Zhang, Y. He and Q. Gao, *Mater. Des.*, 2020, **192**, 108757.
24 C. C. Wang, J. Y. Chen and J. Wang, *J. Biomed. Mater. Res., Part A*, 2022, **110**, 204–216.
25 Y. Zhao, Y. Li, S. Mao, W. Sun and R. Yao, *Biofabrication*, 2015, **7**, 045002.
26 S. H. Kim, Y. K. Yeon, J. M. Lee, J. R. Chao, Y. J. Lee, Y. B. Seo, M. T. Sultan, O. J. Lee, J. S. Lee, S. I. Yoon, I. S. Hong, G. Khang, S. J. Lee, J. J. Yoo and C. H. Park, *Nat. Commun.*, 2018, **9**, 1620.
27 K. Yu, X. Zhang, Y. Sun, Q. Gao, J. Fu, X. Cai and Y. He, *Bioact. Mater.*, 2022, **11**, 254–267.
28 A. Singh, S. Asikainen, A. K. Teotia, P. A. Shiekh, E. Huotilainen, I. Qayoom, J. Partanen, J. Seppälä and A. Kumar, *ACS Appl. Mater. Interfaces*, 2018, **10**, 43327–43342.
29 R. López-Cebral, J. Silva-Correia, R. L. Reis, T. H. Silva and J. M. Oliveira, *ACS Biomater. Sci. Eng.*, 2017, **3**, 3098–3122.
30 B. J. Green, K. S. Worthington, J. R. Thompson, S. J. Bunn, M. Rethwisch, E. E. Kaalberg, C. Jiao, L. A. Wiley, R. F. Mullins, E. M. Stone, E. H. Sohn, B. A. Tucker and C. A. Guymon, *Biomacromolecules*, 2018, **19**, 3682.
31 Z. Zhang, M. L. Jørgensen, Z. Wang, J. Amagat, Y. Wang, Q. Li, M. Dong and M. Chen, *Biomaterials*, 2020, **253**, 120108.
32 X. Fang, H. Guo, W. Zhang, H. Fang, Q. Li, S. Bai and P. Zhang, *J. Mater. Chem. B*, 2020, **8**, 10593–10601.
33 J. Wang, Y. Cheng, H. Wang, Y. Wang, K. Zhang, C. Fan, H. Wang and X. Mo, *Acta Biomater.*, 2020, **117**, 180–191.
34 S. Vijayavenkataraman, S. Thaharah, S. Zhang, Z. Shuo, F. L. Wen and Y. H. F. Jerry, *Mater. Des.*, 2019, **162**, 171–184.
35 S. Vijayavenkataraman, S. Thaharah, S. Zhang, Z. Shuo, F. L. Wen and Y. H. F. Jerry, *Artif. Organs*, 2019, **43**, 515–523.
36 S. Yang, J. Zhu, C. Lu, Y. Chai, Z. Cao, J. Lu, Z. Zhang, H. Zhao, Y. Y. Huang, S. Yao, X. Kong, P. Zhang and X. Wang, *Bioact. Mater.*, 2022, **8**, 529–544.
37 Y. Li, S. Lv, H. Yuan, G. Ye, W. Mu, Y. Fu, X. Zhang, Z. Feng, Y. He and W. Chen, *Adv. Funct. Mater.*, 2020, **31**, 2010215.
38 K. Arcaute, B. K. Mann and R. B. Wicker, *Tissue Eng., Part C*, 2011, **17**, 27–38.
39 L. Yao, G. C. de Ruiter, H. Wang, A. M. Knight, R. J. Spinner, M. J. Yaszemski, A. J. Windebank and A. Pandit, *Biomaterials*, 2010, **31**, 5789–5797.
40 T. M. Dinis, R. Elia, G. Vidal, Q. Dermigny, C. Denoeud, D. L. Kaplan, C. Egles and F. Marin, *J. Mech. Behav. Biomed. Mater.*, 2015, **41**, 43–55.
41 X. Hu, J. Huang, Z. Ye, L. Xia, M. Li, B. Lv, X. Shen and Z. Luo, *Tissue Eng., Part A*, 2009, **15**, 3297–3308.
42 H. Xuan, S. Wu, Y. Jin, S. Wei, F. Xiong, Y. Xue, B. Li, Y. Yang and H. Yuan, *Adv. Sci.*, 2023, **10**, e2302519.
43 X. Dong, Y. Yang, Z. Bao, A. C. Midgley, F. Li, S. Dai, Z. Yang, J. Wang, L. Liu, W. Li, Y. Zheng, S. Liu, Y. Liu, W. Yu, J. Liu, M. Fan, M. Zhu, Z. Shen, G. Xiaosong and D. Kong, *Bioact. Mater.*, 2023, **30**, 98–115.
44 Q. Zhang, Z. Tong, F. Chen, X. Wang, M. Ren, Y. Zhao, P. Wu, X. He, P. Chen and Y. Chen, *J. Neural. Eng.*, 2020, **17**, 036003.